DR RICHARD M LAINE (Orcid ID : 0000-0003-4939-3514)

Article type : Article

Corresponding author mail id: talsdad@umich.edu

Photocatalytic plate-like $La_2Ti_2O_7$ nanoparticles synthesized via liquid-feed flame spray pyrolysis (LF-FSP) of metalloorganic precursors.

Yoshiyuki Abe[1,2] and Richard M. Laine[1*]

[1] Department of Materials Science and Engineering, University of Michigan, Ann Arbor, MI 48109-2136 USA.

[2] Ichikawa Research Center, Sumitomo Metal Mining Co., Ltd., Nakakokubun, Ichikawa, Chiba 272-8588 Japan.

*Corresponding author.

Abstract

Nanoparticles (NPs) of a perovskite-slab-type oxide, $La_2Ti_2O_7$, were synthesized using LF-FSP coupled with subsequent heat-treatments, and their photocatalytic activity was evaluated using decolorization of methyl orange solution under Uv irradiation. The LF-FSP process uses metalloorganic precursors to produce NPs with very low agglomeration with average particle sizes (APSs) of 26 nm (LF-FSP NP). Optimized heat-treatment of these NPs at 1000 ˚C/3h/air gave small, plate-like NPs with high crystallinity, and BET specific surface areas (SSAs) of 14 m^2/g, that exhibited the best observed photocatalytic activity. High-angle annular dark-field scanning TEM shows that heat-treating eliminates microstructural defects in these NPs, improving photocatalytic activity by ≈30 %. The current approach to perovskite-slab-type NPs using LF-FSP provides a simple route to materials with superior photocatalytic activity and offers the advantage of good productivity, 30 g/h.

Key words: Liquid-feed flame spray pyrolysis, nanoparticle, photocatalyst, perovskite-slab-type compound, $La_2Ti_2O_7$

1. Introduction

Liquid-feed flame spray pyrolysis (LF-FSP) is a unique approach to obtaining ceramic nanopowders (NPs) via aerosolization of alcohol solutions containing controlled concentrations of mixtures of metalloorganic compounds into a flame in flowing oxygen carrier gas that is ignited using methane/oxygen torches generating a cloud of ions at ≈ 1200 °C. This cloud is quickly quenched to produce unaggregated NPs typically with the same composition as in the original solution[1,2] without using hot

surfaces as the heat source.[3] LF-FSP gives ≈ 30 g/h NPs. LF-FSP processed NPs typically offer APSs of 25-70 nm and narrow size distributions not easily obtained using precipitation methods with conventional metal salts such as nitrates and chlorides.[4] Moreover, owing to rapid quenching, the largely unaggregated NPs are readily dispersable providing access to a wide variety of thin, dense, flexible and functional, thin ceramic films, 5-60 μm.[5-8]

The work reported here concerns the LF-FSP synthesis of perovskite-related layered compounds that have attracted considerable attention because of their multiple interesting properties, such as high temperature superconductivity,[9,10] ferroelectricity,[11,12] ferromagnetism[13,14] and photocatalytic activity.[15,16] They can be classified into three main groups[17,18]; Ruddlesden-Popper- ($A_{m+1}B_mO_{3m+1}$), Aurevilleus- ($A_{m-1}Bi_2B_mO_{3m+3}$) and perovskite-slab-type ($A_mB_mO_{3m+2}$). In all types, A is a large 12 co-ordinate cation, B is a small 6 co-ordinate cation and the layers are *m* BO_6 octahedra thick.

$La_2Ti_2O_7$, the focus here, belongs to the perovskite-slab group. $La_2Ti_2O_7$ is a well-known ferroelectrics having a Curie temperature of 1773 K.[19-21] Several different values for its band gap (3.29-4.05 eV) have been reported.[22-25] Kim et al.[26] first reported that $La_2Ti_2O_7$ could be used to photocatalytically split water under UV light. Periodically arranged corner-shared TiO_6 octahedra boost charge mobility providing quantum yields as high as 27% especially for Uv promoted photocatalytic water splitting.[24,27]

Several approaches to properties improvement have been studied including solid-state reactions,[28] polymerizable complex methods,[27,29,30] spray pyrolysis,[31] metalloorganic decomposition,[32] hydrothermal[33-35] and flux synthesis methods[36-38].

Furthermore, N-doping has been explored targeting visible-light photocatalytic behavior.[38,39]

In this study, we first synthesized the perovskite-slab-type $La_2Ti_2O_7$ NPs using LF-FSP from simple metalloorganic precursors coupled with a post heat-treatment providing access to suitable materials whose photocatalytic activity for degradation of methyl orange solutions was subsequently examined. In particular, we are able to process $La_2Ti_2O_7$ NPs with high crystallinity and large surface areas from the flame made NPs and compare their characteristics with materials prepared by other methods reported previously.

2. Experimental

2.1 NPs syntheses through LF-FSP

NPs were prepared via LF-FSP using the metalloorganic precursors; lanthanum isobutyrate $\{La[O_2CCH(CH_3)_2]_3\}$ and triethanolamine titanate ($C_6H_{17}NO_6Ti$). Triethanolamine titanate was purchased (MP Biomedicals, LLC, technical grade). Lanthanum isobutyrate was synthesized by reaction of lanthanum oxide with isobutyric acid. The detailed conditions are described in our previous paper.[5]

$$La_2O_3 + 6\ C_3H_7CO_2H \rightarrow La[O_2CCH(CH_3)_2]_3 + 3H_2O$$

The ceramic yields of each precursor were measured by TGA.[5] The precursors were dissolved in ethanol at stoichiometric molar ratios (La:Ti = 1:1) to give a 3 wt. % ceramic yield solution. The precursor solution was aerosolized with oxygen with flow speed of 50 mL/min into a stainless steel chamber where it was combusted with methane/oxygen pilot torches in an oxygen rich environment. Combustion of solvent and organic ligands creates a plume of ions that are quenched and quickly condense to

unaggregated NPs were collected down-stream in rod-in-tube electrostatic precipitators operated at 10 kV. Figure 1 presents a schematic of the apparatus. The LF-FSP process was detailed in a previous paper.[1]

The NPs were then heat-treated at 900-1200˚C/0-6h/air using an electric furnace (MTI Corporation, GSL1600X) to optimize photocatalytic properties.

2.2 Characterization

Powder X-ray diffraction (XRDs) analyses were run on a Rigaku Rotating Anode Goniometer for simple phase determination of the NPs. Scans were from 10 to 70˚ 2θ, using graphite-monochromator-filtered CuKα radiation operating at 40 kV and 100 mA.

Fourier transform infrared (FTIR) spectra were recorded using Nicolet 6700 Series FTIR spectrometer (Thermo Fisher Scientific, Inc.) in KBr dispersions in the range of 400 - 4000 cm^{-1}.

Brunauer-Emmett-Teller (BET) surface areas were determined using ASAP 2020 sorption analyzer (Micrometrities Inst.) from nitrogen adsorption isotherms and using AS1-MP and AS-iQ sorption analyzer (Quantachrome Inst.) from krypton adsorption isotherms. Scanning electron microscopy (SEMs) were run on a JEOL JSM-IT500 to observe the NPs. All samples were sputter coated with Au/Pd using a SPI sputter coater. Average particle sizes (APSs) of LF-FSP NPs were determined from size measurement of more than 100 particles in the SEM images.

Transmission electron microscope (TEM) and a high-angle annular dark-field scanning transmission electron microscopy (HAADF-STEM) were run at 200 kV on JEOL JEM-ARM200F for observation of microstructure of the NPs. Selected area electron diffraction (SAED) was also run to estimate crystallinity.

X-ray photoelectron spectroscopy (XPS) analysis was run on ULVAC-PHI Versa Prove II for investigation of surface defects of the NPs.

UV-vis diffused reflectance spectra analysis was run on a Hitachi UH4150 spectrophotometer equipped with an integrating sphere to estimate a bandgap energy of the NPs.

2.3 Photocatalytic evaluation

Photocatalytic activity was evaluated quantitatively by decolorization of methyl orange (MO) solutions with NP dispersions under UV irradiation. 15 mg of NPs were put into 15 g of 0.001 w/v % methyl orange solution, followed by ultrasonic dispersion for 5 min to obtain a suspension. Afterwards, the suspension was placed in a dark place for 1 h to adjust the powder surface to the solution. Then it was irradiated under UV by using a light source of 400W metal halide lamp for 0 - 60 min. The distance between the light source and the sample was 230 mm, and the suspension was not stirred but cooled during the irradiation. The suspended state could be kept up after the irradiation owing to the small size of the NPs.

The suspension was then transferred to a vial and centrifuged for 30 min. Then, the wavelength dependent absorbance of the supernatant was measured using a UV-vis spectrophotometer (Agilent Cary 60). Absorbance of the MO solution at 464 nm was measured and calibrated by a plot of the absorbance at 464 nm as a function of the MO solution to obtain the MO concentration (C). Decolorization degree was estimated from calculating $((C_0\text{-}C)/C_0) \times 100$ (%), where C_0 is initial MO concentration (0.001 w/v (%)). We confirmed almost no decolorization obtains without any photocatalyst, as a reference.

3. Results and discussion

3.1 LF-FSP NPs

Figure 2a provides SEMs of as synthesized NPs; consisting of small primary particles with APSs of ≈ 26 nm, low agglomerate contents and no apparent necking. Note that the small primary particles do not form agglomerated large (> 1μm) secondary particles, as often observed in conventional spray pyrolysis products.[3,40] The BET surface area was measured as 27 m^2/g.

A TEM image of the NPs is provided in Figure 2b, showing spherical facetted particles. Figures 2c and d provide HAADF-STEM images of areas 1 and 2 in Figure 2b respectively. It can be seen that the NPs exhibit twin deformation (yellow arrow in Figure 2c) and irregular lattice disorder (red arrows in Figure 2d). Such microstructural defects are likely ascribed to NP formation through quenching from a cloud of gaseous ions at high temperatures in very short times.

The Figure 3 XRD pattern exhibits diffraction peaks identified as $La_2Ti_2O_7$ (PDF#01-081-1066: $P2_1$-type, monoclinic). Fluctuations in the lattice spacing due to the microstructural defects (Figure 2c, d.) and the low crystallinity broaden the diffraction peaks. Some multiple neighboring peaks seem to be connected to show single strong peaks. Ishizawa et al.[41] reported that the high temperature phase of $La_2Ti_2O_7$ (PDF#04-008-8491: $Cmc2_1$-type, orthorhombic) is formed above approximately 780 ˚C. This phase was not evident in our samples even though the NPs were formed by quenching from high temperature.

3.2 Heat-treatment of NPs

It is known that high crystallinity (low defect densities), high dispersion and large surface areas favor superior photocatalytic activity as they minimize non-radiative decay processes.[42] Thus, we explore heat-treating the NPs. To suppress the significant decrease in high dispersion and large SSAs, we explored heating at modest temperatures. Figure 4 provides XRDs for NPs heat-treated at 900-1000˚C/0h/air at 10˚C/min. Although diffraction peak shapes remain unchanged at heat-treatments below 950 ˚C, they began to change at 1000 ˚C, implying that diffusion leading to crystal growth commences. Therefore, we heat-treated the NPs at 1000˚C at 0.5, 1.5, 3.0, 4.5 and 6.0 h. All diffraction peaks could be clearly indexed to monoclinic $La_2Ti_2O_7$ with $P2_1$-type space group (PDF#01-081-1066) for all heat-treated samples. A typical XRD for NPs heat-treated at 1000˚C/3h/air is shown in Figure 5.

The FT-IR spectrum of NPs heat-treated at 1000˚C/3h/air in KBr is provided in Figure 6. The spectra show two strong, broad absorption bands around 561 and 653 cm^{-1}, attributed to νTi-O in TiO_6 octahedra and νLa-O, respectively.[43,44] Absorption bands around 466 cm^{-1} are also found for νLa-O. Furthermore, small bands around 766 and 808 cm^{-1} can be due to one short νTi-O bond in TiO_5 and TiO_4 units, respectively.[45]

Figure 7a-c provide SEM images of NPs heat-treated at 1000˚C/1.5h/air, 1000˚C/3h/air and 1000˚C/6h/air, showing that the size is increased with increase in the heat-treatment time. The NPs heat-treated at 1000˚C/3h/air (Figure 7b) have plate-like morphologies approximately 100 nm in diameter and 20-30 nm thick. Weak aggregation seems to be maintained even after heat-treatment. Figure 7d shows a TEM of the NPs, showing that the plate-like NPs are necked at the edges of each NP. HAADF-STEM image of area 1 in d and SAED of area 2 in d are shown in Figure 7e and f, respectively. It can be seen that the high crystallinity with a regular array of

lattice planes and no defects results following heat-treatment.

The surface oxygen defect of the LF-FSP NPs and the NPs heat-treated at 1000˚C/3h/air was investigated by XPS analysis. Figure 8 provides the results around O1s region, showing the spectra at the binding energy of 529.5, 531.4 and 532.9 eV in the both samples. The binding energy at 529.5 eV is ascribed from O-Ti^{4+} in the crystal lattice and those at 531.4 and 532.9 eV are attributed to surface adsorbed hydroxyl groups.[46-47] Considering that physically absorbed hydroxyl groups on the samples must be eliminated in the ultrahigh vacuum condition of XPS apparatus, these signals can be said to be attributed to Ti-OH and H_2O, which are strongly bounded to surface defects.[47-49] Figure 8 clearly reveals that the spectra at 531.4 and 532.9 eV in the LF-FSP NPs are higher than those in the NPs heat-treated at 1000˚C/3h/air, indicating the higher surface defect in the LF-FSP NPs.

The BET SSA for NPs heat-treated at 1000˚C/3h/air was 14 m^2/g. Kim et al.[27] reported synthesizing $La_2Ti_2O_7$ by a polymerizable complex (PC) and solid-state reaction (SSR) methods finding much lower SSAS of 5-8 m^2/g from the PC method with heat-treatment at 950-1050 ˚C/2h and after heat-treating at 1150˚C/24h to generate single phase materials with SSAs of 1 m^2/g. We believe that the limited aggregation (low bulk density) of LF-FSP NPs (Figure 2a) likely suppresses necking, grain growth and thus loss of surface area.

In addition to conventional spray pyrolysis, SSR and PC methods, several other approaches to synthesize $La_2Ti_2O_7$ have been reported. Metalloorganic deposition[32] yields highly aggregated powder. The flux method[36-38] provides photocatalytically active, plate-like crystals but with large particle sizes (~ μm). Hydrothermal synthesis produces thin nanosheets.[33,34,39] The hydrothermal method is not suitable for

mass-production because of the times involved. Compared with the other methods, it can be said that LF-FSP offers characteristics of small plate-like $La_2Ti_2O_7$ NPs with high crystallinity and high SSAs.

3.3 Photocatalytic properties

Figure 9 provides the UV-vis diffuse reflectance spectra for LF-FSP NP (blue dotted line) and for NPs heat-treated at 1000 ˚C/3h/air (red solid line). The reflectance coefficient was converted to adsorption using the Kubelka-Munk function. The bandgap energy was estimated to be 3.87 eV for the LF-FSP NPs and 4.00 eV for the heat-treated ones from the absorption edges. These values are in good agreement with those reported previously.[22-25] Therefore, we confirm that the samples readily absorb UV light.

Dai et al.[50] reported that mesoporous titania NPs causes photocatalytic decomposition of the MO in water under UV irradiation leading to decolorization of the MO solutions. Thus, quantitative evaluation of the photocatalytic activity can be carried out by measuring decolorization of MO solutions with the photocatalyst under UV irradiation. Since MO has good resisting property toward the UV light, use of it has an advantage to evaluate photocatalytic activity of catalysts under the UV irradiation precisely.

Figure 10a shows the absorbance spectra of an MO solution with NPs heat-treated at 1000˚C/3h/air after UV irradiation for different times (0-60 min). The MO concentration (C) after irradiation was estimated from the absorbance at 464 nm and the decolorization degree $((C_0\text{-}C)/C_0) \times 100$ (%), C_0: initial MO concentration) was calculated. Figure 10b provides a dependence of the decolorization degree on UV irradiation time for NPs heat-treated at 1000˚C/3h/air. It can be seen that the

decolorization degree increases monotonically with increases in irradiation time. Next, we examined the catalytic activity of the NPs heat-treated at 1000˚C for different times (0-6h) in air by using the decolorization of the MO solution. Figure 10c provides absorbance spectra of the MO solution after UV irradiation with LF-FSP NP and NPs heat-treated at 1000˚C/0.5-6h/air. The UV irradiation time was 1h. Similarly, the decolorization degree of MO, which imply the photocatalytic activity in this case, was evaluated from the spectra, and their dependences on the heat treatment time was derived, which is shown in Figure 10d. This figure also provides a dependence of BET SSAS of NPs and heat-treating time. In the figure, the data at 0 h are for the LF-FSP NPs. Although the BET surface area decreased monotonically with the heat-treating time, the highest photocatalytic activity was obtained at 3 h. For heat-treating times shorter than 3 h, the BET surface area decreased while the photocatalytic activity increased. Yan et. al.[49] described that the surface defects of TiO_2, that is, oxygen vacancy clusters, could promote the separation of electron-hole pairs under irradiation, which leads to enhancement of the photocatalytic activity. As described above, the surface defect evaluated from XPS of O1s in the LF-FSP NPs decreased by the heat-treating at 1000˚C/3h/air. Therefore, it can be said that the surface defect is not dominant for the photocatalytic activity as for our samples. The reason might be due to improvements in the crystallinity and interior defect density reductions.[42] Improvement in the crystallinity enhances the mobility of electrons and holes and reduction in the defect suppresses recombination of electrons and holes.

In contrast, in the range of the heat-treating times longer than 3 h, photocatalytic activity decreased monotonically with time. This might arise from decreases in surface

area. Therefore, best photocatalytic activity could be obtained from NPs heat-treated at 1000˚C/3h/air, which still offer large surface area of 14 m^2/g.

4. Conclusions

In this study, perovskite-slab-type $La_2Ti_2O_7$ NPs were synthesized using LF-FSP of metalloorganic precursors of lanthanum isobutyrate and triethanolamine titanate coupled with a subsequent heat-treatment at 1000 ˚C/air. The LF-FSP NPs had characteristically low agglomeration of primary particles with APSs of 26 nm and large SSAs of 27 m^2/g. Heat-treatment at 1000 ˚C/3h/air resulted in formation of plate-like single crystal NPs while still retaining SSAs of 14 m^2/g while eliminating microstructural defects thereby optimizing photocatalytic activity. Finally, this work introduces LF-FSP processing of perovskite-slab-type NPs with high crystallinity and high surface area for photocatalytic applications.

Acknowledgement

We thank Sumitomo Metal Mining Co., Ltd. (Japan) for funding a one-year visiting scientist position for Dr. Abe and funds to complete the work reported here.

References

1. Bickmore CR, Waldner KF, Baranwal R, Hinklin T, Treadwell DR, Laine RM. Ultrafine titania by flame spray pyrolysis of a titanatrane complex. J Euro Ceram Soc. 1998, 18 (4) 287-297.

2. Laine RM, Marchal JC, Sun HP, Pan XQ. Nano-α-Al_2O_3 by liquid-feed flame spray pyrolysis. Nat Mater. 2006, 5 710-712.

3. Messing GL, Zhang S-C, Jayanthi GV. Ceramic powder synthesis by spray pyrolysis. J Am Ceram Soc. 1993, 76 (11) 2707-2726.

4. Hinklin T, Toury B, Gervais C, Babonneau F, Gislason JJ, Morton RW, et. al. Liquid-feed flame spray pyrolysis of metalloorganic and inorganic alumina sources in the production of nanoalumina powders. 2004, Chem Mater. 16 (1) 21-30.

5. Yi E, Wang W, Kieffer J, Laine RM. Flame made nanoparticles permit processing of dense, flexible, Li^+ conducting ceramic electrolyte thin films of cubic-$Li_7La_3Zr_2O_{12}$ (c-LLZO). J Mater Chem A. 2016, 4 (33) 12947-12954.

6. Yi E, Wang W, Kieffer J, Laine RM. Key parameters governing the densification of cubic- $Li_7La_3Zr_2O_{12}$ Li^+ conductors. 2017, J Power Sources. 352 (1) 156-164.

7. Yi E, Temeche E, Laine RM. Superionically conducting β''-Al_2O_3 thin films processed using flame synthesized nanopowders. 2018, J Mater Chem A. 6 (26) 12411-12419.

8. Abe Y, Yi E, Laine RM. Processing thin, dense, transparent Ce:$Y_3Al_5O_{12}$ films from flame made nanopowders for white light applications. J Euro Ceram Soc. 2019, 39 (15) 4972 - 4978.

9. Bednorz JG, Müller KA. Possible high Tc superconductivity in the Ba-La-Cu-O system. Z Physik. B 1986, 64 189-193.

10. Wu MK, Ashburn JR, Torng CJ, Hor PH, Meng RL, Gao L, et al. Superconductivity at 93 K in a new mixed-phase Y-Ba-Cu-O compound system at ambient pressure. Phys Rev Lett. 1987, 58 (9) 908-910.

11. Mulder AT, Benedek NA, Rondinelli JM, Fennie CJ, Turning ABO_3 antiferroelectrics into ferroelectrics: design rules for practical rotation-driven ferroelectricity in double perovskites and $A_3B_2O_7$ Ruddlesden-Popper compounds. Adv Fun Mater. 2013, 23 (38) 4810-4820.

12. Amanuma K, Hase T, Miyasaka Y, Preparation and ferroelectric properties of $SrBi_2Ta_2O_9$ thin films. Appl Phys Lett. 1995, 66 (2) 221-223.

13. Mao X, Wang W, Chen X, Lu Y, Multiferroic properties of layer-structured $Bi_5Fe_{0.5}Co_{0.5}Ti_3O_{15}$. Appl Phys Lett. 2009, 95 082901/1-3.

14. Keeney L, Maity T, Schmidt M, Amann A, Deepak N, Petkov N, et al. Magnetic field-induced ferroelectric switching in multiferroic aurivillius phase thin films at room temperature. J Am Ceram Soc. 2013, 96 (8) 2339-2357.

15. Shimizu K, Itoh S, Hatamachi T, Kodama T, Sato M, Toda K. Photocatalytic water

splitting on Ni-intercalated Ruddlesden−Popper tantalate $H_2La_{2/3}Ta_2O_7$, Chem Mater. 2005, 17 (20) 5161-5166.

16. Machida M, Yabunaka J, Kijima T. Synthesis and photocatalytic property of layered perovskite tantalates, $RbLnTa_2O_7$ (Ln = La, Pr, Nd, and Sm). Chem Mater. 2000, 12 (3) 812-817.

17. Isupov VA. Crystal chemical aspects of the layered perovskite-like oxide ferroelectrics of the $AnMnO_3n_2$ type. Ferroelectrics. 1999, 220 (1) 79-103.

18. Lichtenberg F, Herrnberger A, Wiedenmann K, Mannhart J. Synthesis of perovskite-related layered $A_nB_nO_{3n+2} = ABO_X$ type niobates and titanates and study of their structural, electric and magnetic properties. Progress in Solid State Chem. 2001, 29 (1-2) 1-70.

19. Nanamatsu S, Kimura M, Doi K, Matsushita S, Yamada N. A new ferroelectric: $La_2Ti_2O_7$. Ferroelectrics. 1974, 8 (1) 511-513.

20. Stefanovich SY, Nanamatsu S, Venevtsev YN. Photovoltaic properties and photoconductivity of $A_2B_2O_7$ ferroelectrics. Ferroelectrics. 1980, 29 (1) 59-62.

21. Yamamoto JK, Bhalla AS. Piezoelectric properties of layered perovskite $A_2Ti_2O_7$ (A=La and Nd) single-crystal fibers. J Appl Phys. 1991, 70 (8) 4469-4471.

22. Hwang DW, Lee JS, Li W, Oh SH. Electronic band structure and photocatalytic activity of $Ln_2Ti_2O_7$ (Ln = La, Pr, Nd). J Phys Chem B. 2003, 107 (21) 4963-4970.

23. Uno M, Kosuga A, Okui M, Horisaka K. Yamanaka S. Photoelectrochemical study of lanthanide titanium oxides, $Ln_2Ti_2O_7$ (Ln = La, Sm, and Gd). J Alloys Comp. 2005, 400 (1-2) 270-275.

24. Abe R, Higashi M, Sayama K, Abe Y, Sugihara H. Photocatalytic activity of R_3MO_7 and $R_2Ti_2O_7$ (R = Y, Gd, La; M = Nb, Ta) for water splitting into H_2 and O_2. J Phys Chem B 2006, 110 (5) 2219-2226.

25. Wang Z, Teramura K, Hosokawa S, Tanaka T. Photocatalytic conversion of CO_2 in water over Ag-modified $La_2Ti_2O_7$. Appl Cat B: Environ. 2015, 163 241-247.

26. Kim HG, Hwang DW, Kim J, Kim YG, Lee JS. Highly donor-doped (110) layered perovskite materials as novel photocatalysts for overall water splitting. Chem Commun. 1999, (12) 1077-1078.

27. Kim HG, Hwang DW, Bae SW, Jung JH, Lee JS. Photocatalytic water splitting over $La_2Ti_2O_7$ synthesized by the polymerizable complex method. Catal Lett. 2003, 91 (3-4) 193-198.

28. Ku Y, Wang LC, Ma CM. Photocatalytic Oxidation of Isopropanol in Aqueous Solution Using Perovskite - Structured $La_2Ti_2O_7$. Chem Eng Technol. 2007, 30 (7)

895-900.

29. Hou WM, Ku Y. Synthesis and characterization of $La_2Ti_2O_7$ employed for photocatalytic degradation of reactive red 22 dyestuff in aqueous solution. J Alloys Comp. 2011, 509 (19) 5913-5918.

30. Rahimi-Nasrabadi M, Mahdavi S, Adib K. Photocatalytically active $La_2Ti_2O_7$ nanostructures, synthesis and characterization. J Mater Sci: Mater Electron. 2017, 28 (17) 12564-12571.

31. Rugen EE, Koczkur KM, Skrabalak SE. Facile synthesis of porous La-Ti-O and $LaTiO_2N$ microspheres. Dalton Trans. 2017, 46 (32) 10727-10733.

32. Zhao Z, Zhang Y, Yang J, Li H, Song W, Zhao X. Low-temperature synthesis of $La_2Ti_2O_7$ nanocrystal by metallorganic decomposition method. J Ceram Soc Jpn. 2005, 113 (1313) 67-70.

33. Chen D., Xu R. Hydrothermal synthesis and characterization of $La_2M_2O_7$ (M= Ti, Zr) powders. Mater Res Bull. 1998, 33 (3) 409-417.

34. Li KW, Wang Y, Wang H, Zhu M, Yan H. Hydrothermal synthesis and photocatalytic properties of layered $La_2Ti_2O_7$ nanosheets. Nanotechnology. 2006, 17 (19) 4863-4867.

35. Onozuka K, Kawakami Y, Imai H, Yokoi T, Tatsumi T, Kondo JN. Perovskite-type $La_2Ti_2O_7$ mesoporous photocatalyst. J Solid State Chem. 2012, 192 87-92.

36. Arney D, Porter B, Greve B, Maggard PA. New molten-salt synthesis and photocatalytic properties of $La_2Ti_2O_7$ particles. J Photochem Photobiol A: Chem. 2008,199 (2-3) 230-235.

37. Hojamberdiev M, Yamaguchi A, Yubuta K, Oishi S, and Teshima K. Fabrication of $La_2Ti_2O_7$ crystals using an alkali-metal molybdate flux growth method and their nitridability to form $LaTiO_2N$ crystals under a high-temperature NH_3 atmosphere. Inorg Chem. 2015, 54 (7) 3237-3244.

38. Wagata H, Zettsu N, Yamaguchi A, Nishikiori H, Yabuta K, Oishi S, et al. Chloride flux growth of $La_2Ti_2O_7$ crystals and subsequent nitridation to form $LaTiO_2N$ crystals. Cryst Growth Des. 2015, 15 (1) 124-128.

39. Meng F, Hong Z, Arndt J, Li M, Zhi M, Yang F, et al. Visible light photocatalytic activity of nitrogen-doped $La_2Ti_2O_7$ nanosheets originating from band gap narrowing. Nano Res. 2012, 5 (3) 213-221.

40. Fuierer PA, Newnham RE, $La_2Ti_2O_7$ Ceramics. J Am Ceram Soc. 1991, 74 (11) 2876-2781.

41. Ishizawa N, Marumo F, Iwai S, Kimura M, Kawamura T. Compounds with

perovskite-type slabs. V. A high-temperature modification of $La_2Ti_2O_7$. Acta Cryst. 1982, B38 (2) 368-372.

42. Maeda K, Domen K. New non-oxide photocatalysts designed for overall water splitting under visible light. J Phys Chem C. 2007, 111 (22) 7851-7861.

43. Chen D, Jiao X, Xu R. Hydrothermal synthesis and characterization of the layered titanates $MLaTiO_4$ (M= Li, Na, K) powders. Mater Res Bull. 1999, 34 (5) 685-691.

44. Last JT. Infrared-absorption studies on barium titanate and related materials. Phys Rev. 1957, 105 (6) 1740-1750.

45. Kartha K, Pai MR, Banerjee AM, Pai RV, Meena SS, Bharadwaj SR, et al. Modified surface and bulk properties of Fe-substituted lanthanum titanates enhances catalytic activity for CO+ N_2O reaction. J Molecular Catalyst A: Chemical. 2011, 335 (1-2) 158-168.

46. Feng W, Wu G, Li L, Guan N. Solvent-free selective photocatalytic oxidation of benzyl alcohol over modified TiO_2. Green Chem. 2011, 13 (11) 3265-3272.

47. Iwabuchi A, Choo C, Tanaka K. Titania nanoparticles prepared with pulsed laser ablation of rutile single crystals in water. J Phys Chem B. 2004, 108 (30) 10863-10871.

48. Wang R, Sakai N, Fujishima A, Watanabe T, Hashimoto K. Studies of surface wettability conversion on TiO_2 single-crystal surfaces. J Phys Chem B, 1999, 103 (12) 2188-2194.

49. Yan J, Wu G, Guan N, Li L, Li Z, Cao X. Understanding the effect of surface/bulk defects on the photocatalytic activity of TiO_2: anatase versus rutile. Phys Chem Chem Phys. 2013, 15 (26) 10978-10988.

50. Dai K, Chen H, Peng T, Ke D, Yi H. Photocatalytic degradation of methyl orange in aqueous suspension of mesoporous titania nanoparticles. Chemosphere 2007, 69 (9) 1361-1367.

Figure captions

Figure 1. Schematic diagram of apparatus of liquid-feed flame spray pyrolysis.

Figure 2a. SEM image and b. STEM image of LF-FSP NP. HAADF-STEM image of c. area 1 and d. area 2 in image b.

Figure 3. XRD pattern of LF-FSP NPs. Lattice planes corresponds to monoclinic $P2_1$-type type $La_2Ti_2O_7$.

Figure 4. XRDs of heat-treated LF-FSP NP.

Heat-treat conditions; a. 1000˚C/0h/air, b. 950˚C/0h/air, c. 900˚C/0h/air.

Temperature raising speed: 10˚C/min.

Figure 5. XRD pattern of NPs heat-treated at 1000˚C/3h/air.

Figure 6. FTIR spectrum of NPs heat-treated at 1000˚C/3h/air.

Figure 7a SEM image and b STEM image of LF-FSP NP heat-treated at 1000 ˚C/3h/air.

c HAADF-STEM image of area 1 in image b and d SAED of area 2 in image b.

Figure 8 XPS of O1s region for (a) LF-FSP NPs and (b) NPs heat-treated at 1000˚C/3h/air.

Figure 9. UV-vis diffused reflectance spectra of LF-FSP NP (blue dotted line) and that heat-treated at 1000˚C/3h/air (red solid line). Inset: plots of $(\alpha h\nu)^2$ *vs.* $h\nu$ to estimate bandgap energy.

Figure 10a. Absorbance spectra of MO solution with NPs heat-treated at 1000˚C/3h/air after UV irradiation for different times.

b. Dependence of degree of decolorization on UV irradiation time for NPs heat-treated at 1000˚C/3h/air.

c. Absorbance spectra of MO solution without NPs and with NPs heat-treated at

1000˚C/0-6h/air after UV irradiation for 1h.

d. Dependence of degree of decolorization and BET surface area on heat-treatment time. Heat-treatment was carried out at 1000 ˚C/air. Uv irradiation time was 60 min.

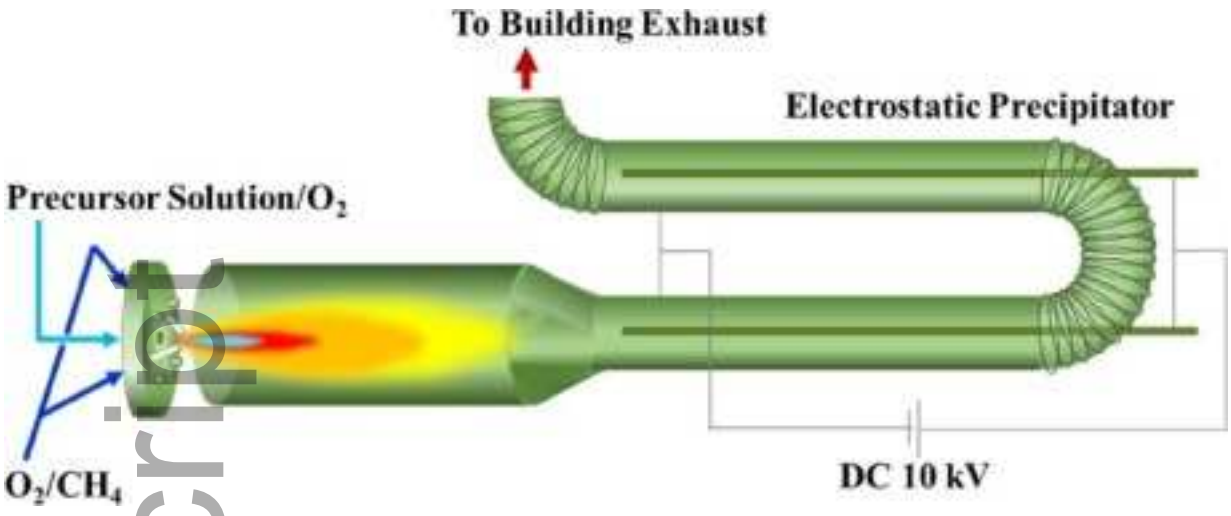

jace_17196_f1.tif

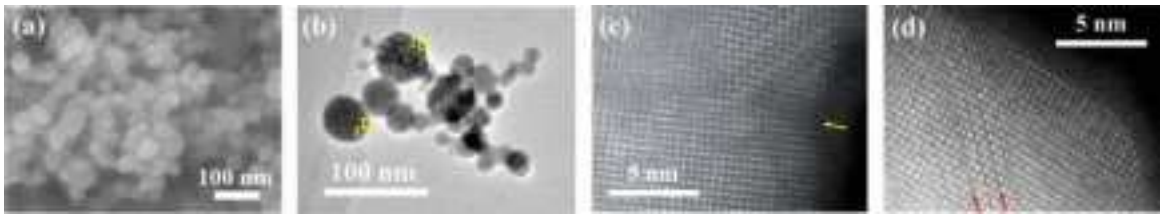

jace_17196_f2.tif

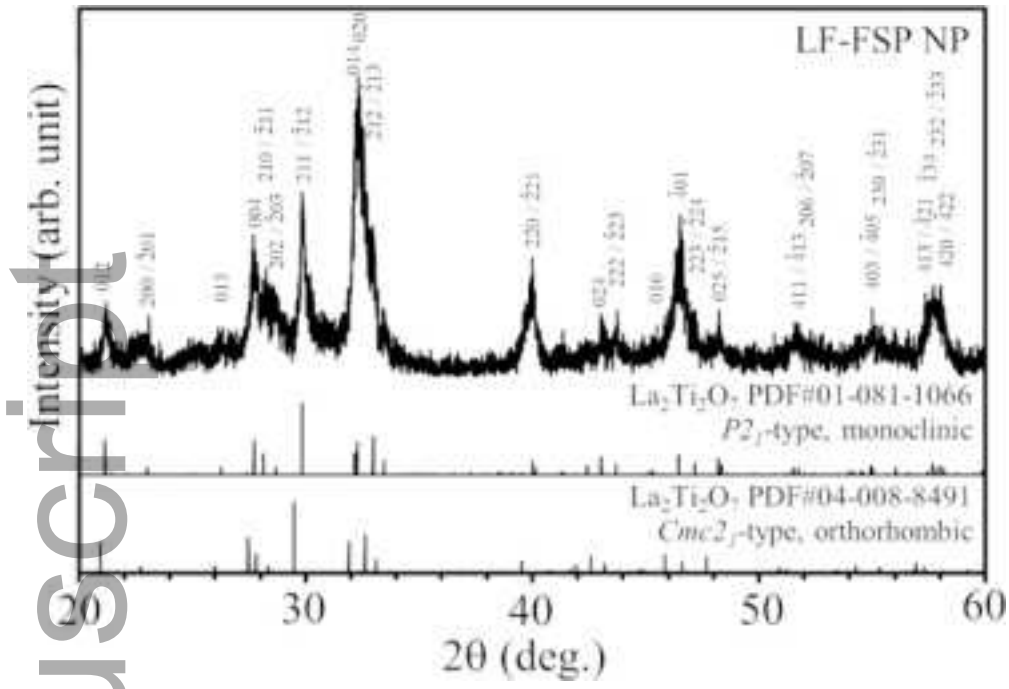

jace_17196_f3.tif

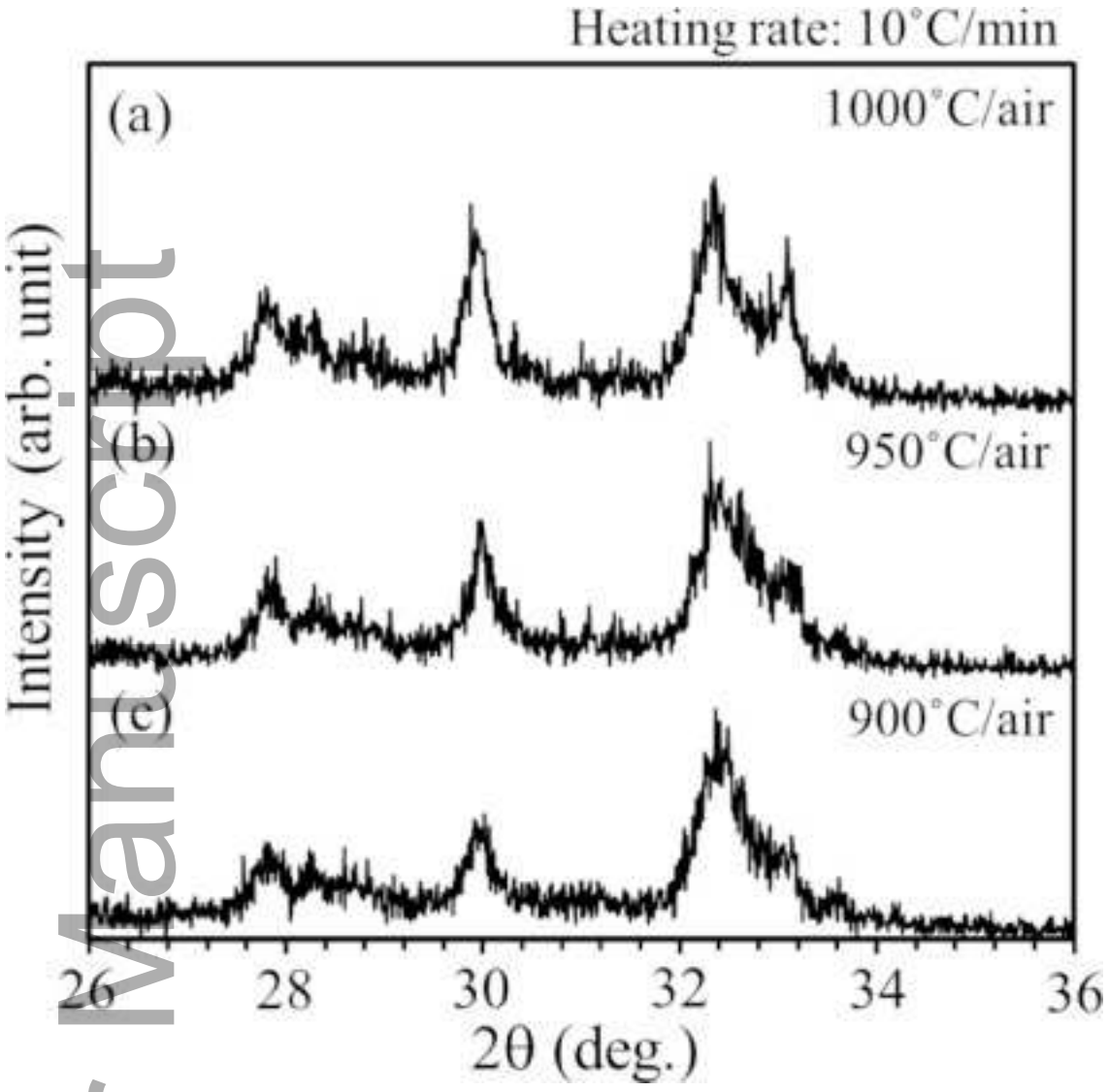

jace_17196_f4.tif

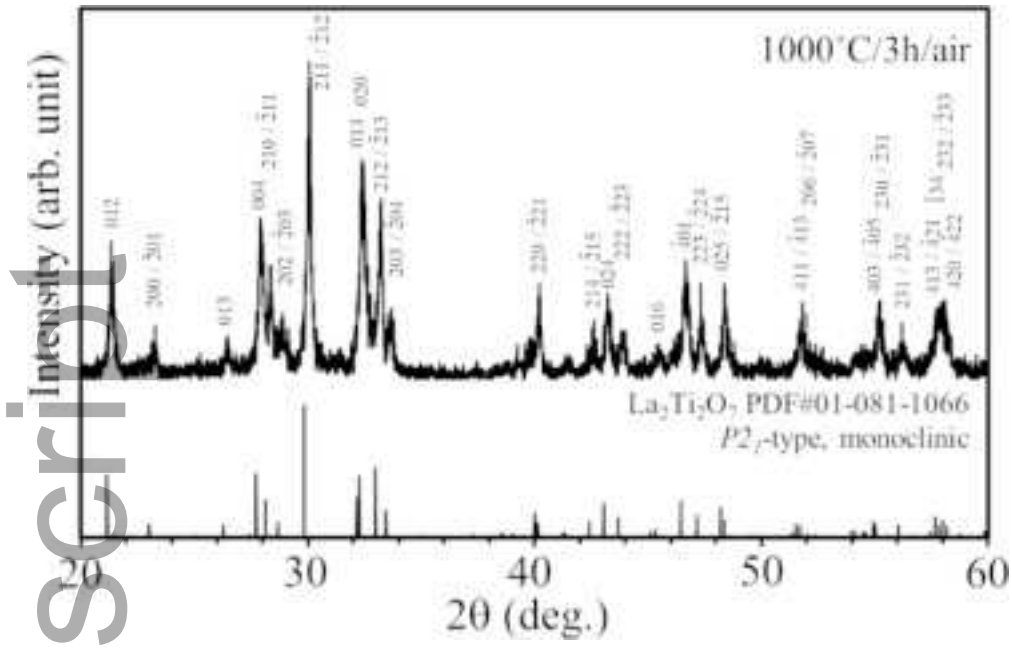

jace_17196_f5.tif

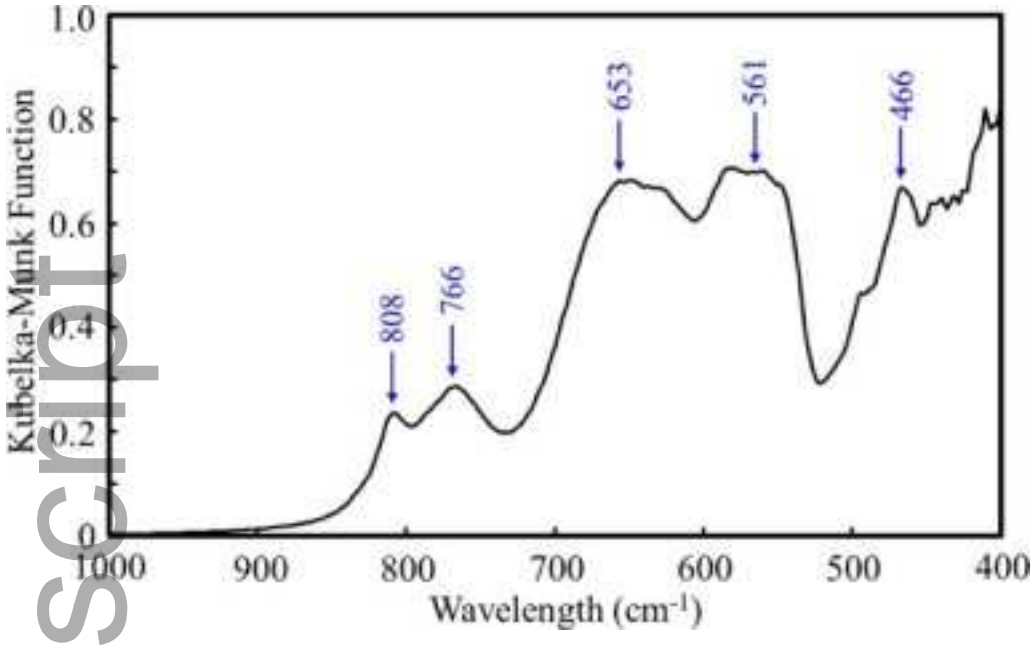

jace_17196_f6.tif

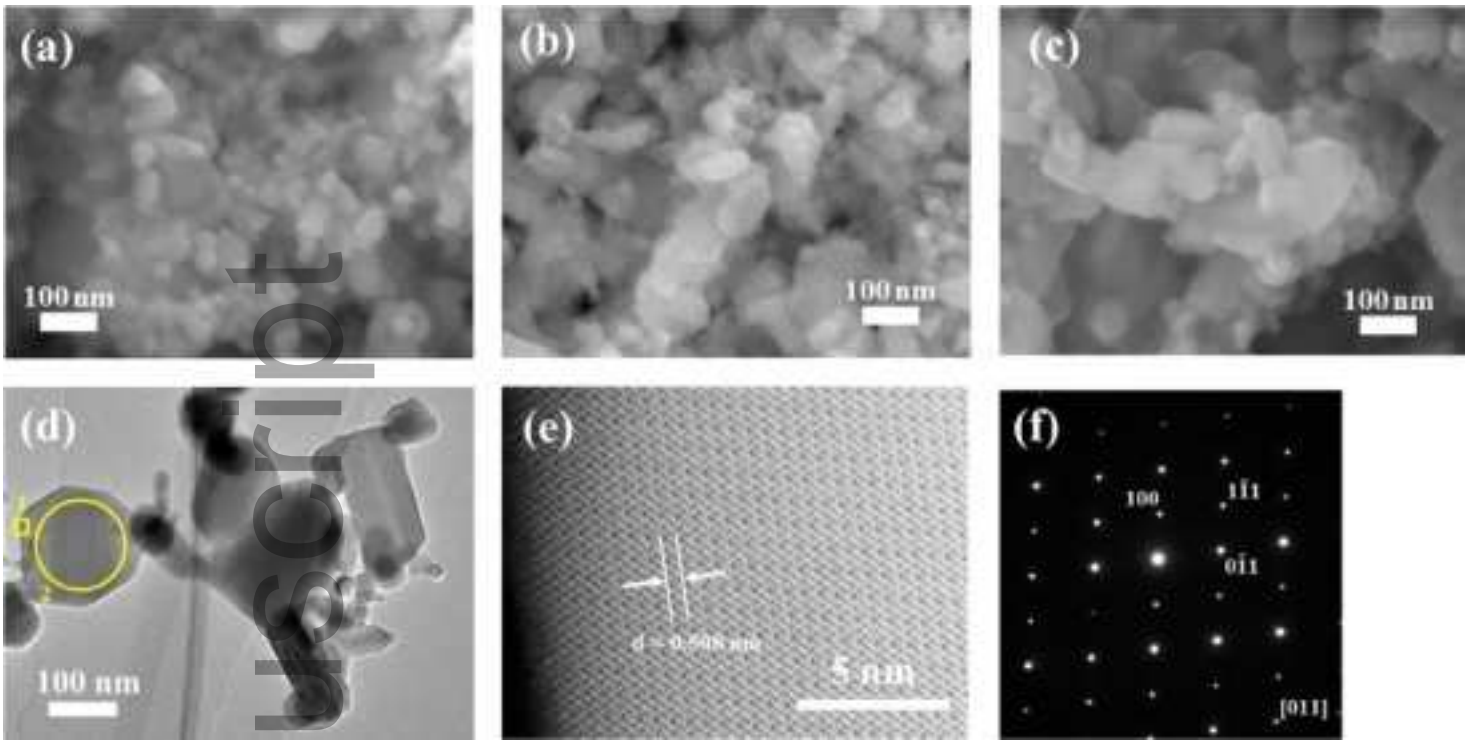

jace_17196_f7.tif

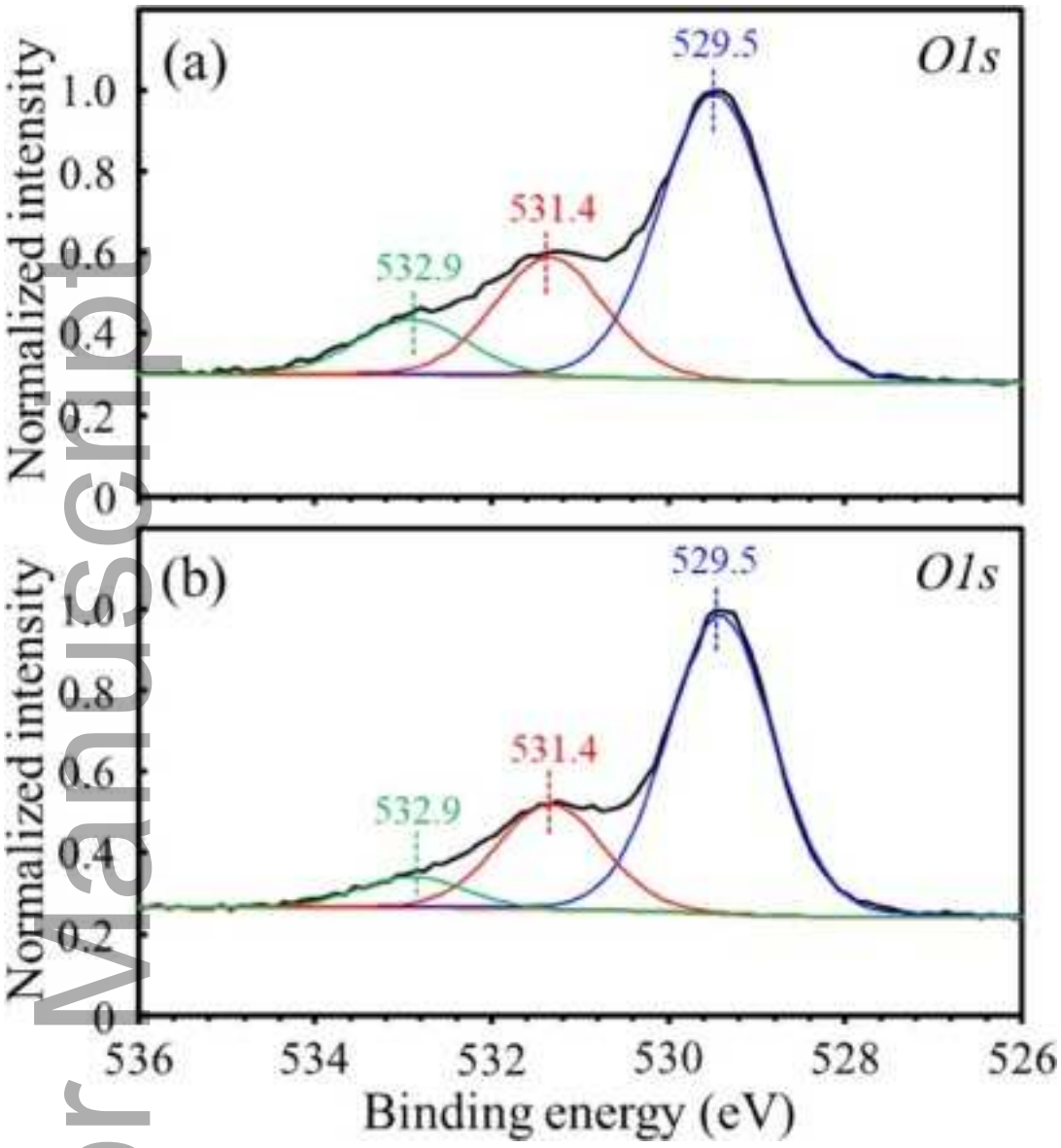

jace_17196_f8.tif

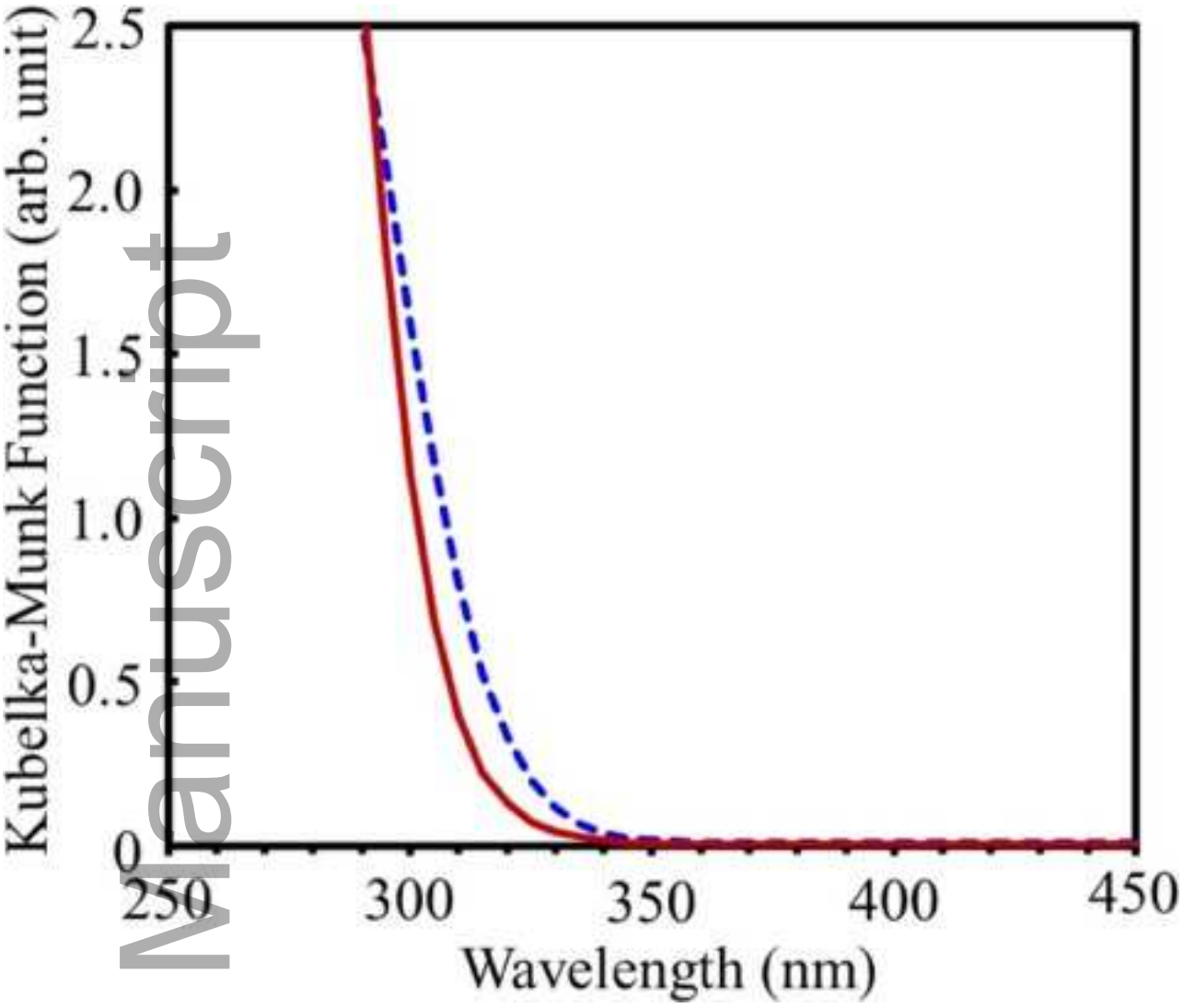

jace_17196_f9.tif

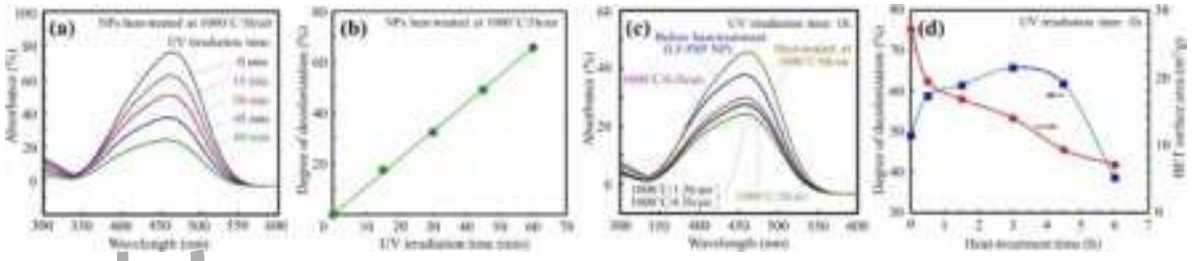

jace_17196_f10.tif